European Journal of Medicinal Chemistry 268 (2024) 116295

Contents lists available at ScienceDirect

European Journal of Medicinal Chemistry

journal homepage: www.elsevier.com/locate/ejmech

Research paper

Synthesis and mitochondria-localized iridium (III) complexes induce cell death through pyroptosis and ferroptosis pathways

Huiyan Hu, Fan Zhang, Zhujun Sheng, Shuang Tian, Gechang Li, Shuanghui Tang, Yajie Niu, Jiawan Yang, Yunjun Liu *

School of Pharmacy, Guangdong Pharmaceutical University, Guangzhou, 510006, PR China

ARTICLE INFO

Keywords:
Iridium(III) complexes
Ferroptosis
RNA-Sequence
Pyroptosis
Antitumor in vivo

ABSTRACT

This paper introduces a new ligand, 4,6-dichloro-5-(1*H*-imidazo [4,5-f]phenanthroline-2-yl)pyrimidin-2-amine (DPPA), and its corresponding new iridium(III) complexes: $[Ir(ppy)_2(DPPA)](PF_6)$ (2a) (where ppy represents deprotonated 2-phenylpyridine), $[Ir(bzq)_2(DPPA)](PF_6)$ (2b) (with bzq indicating deprotonated benzo[h]quinoline), and $[Ir(piq)_2(DPPA)](PF_6)$ (2c) (piq denoting deprotonated 1-phenylisoquinoline). The cytotoxic effects of both DPPA and 2a, 2b, and 2c were evaluated against human lung carcinoma A549, melanoma B16, colorectal cancer HCT116, human hepatocellular carcinoma HepG2 cancer cell lines, as well as the non-cancerous LO2 cell line using the 3-(4,5-dimethylthiazole-2-yl)-2,5-diphenyltetrazolium bromide (MTT) method. While DPPA exhibited moderate anticancer activity toward A549, B16, HCT116 and HepG2 cells, complexes 2a, 2b, and 2c displayed remarkable efficacy against A549, B16, and HCT116 cells. The cell colonies and wound healing were investigated. Moreover, various aspects of the anticancer mechanisms were explored. The cell cycle analyses revealed that the complexes block cell proliferation of A549 cells during the S phase. Complex 2c induce an early apoptosis, while 2a and 2b cause a late apoptosis. The interaction of 2a, 2b and 2c with endoplasmic reticulum and mitochondria was identified, leading to elevated ROS and Ca^{2+} amounts. This resulted in a reduced mitochondrial membrane potential, mitochondrial permeability transition pore opening, and an increase of cytochrome *c*. Also, ferroptosis was investigated through measurements of intracellular glutathione (GSH), malondialdehyde (MDA), and recombinant glutathione peroxidase (GPX4) protein expression. The pyroptosis was explored via cell morphology, release of lactate dehydrogenase (LDH) and expression of pyroptosis-related proteins. RNA sequencing was applied to examine the signaling pathways. Western blot analyses illuminated that the complexes regulate the expression of Bcl-2 family proteins. Additionally, an in vivo antitumor study demonstrated that complex 2c exhibited a remarkable inhibitory rate of 58.58% in restraining tumor growth. In summary, the findings collectively suggest that the iridium(III) complexes induce cell death via ferroptosis, apoptosis by a ROS-mediated mitochondrial dysfunction pathway and GSDMD-mediated pyroptosis.

1. Introduction

Carcinogenesis is believed to arise from DNA alterations within cells, coupled with the inhibition of growth suppressors. These events lead to uncontrollable cell growth, migration to a remote organization, and ultimately result in an aggressive metastasis [1–3]. While cisplatin has demonstrated successful anticancer applications, the clinical utility of cisplatin is curtailed by side-effects [4], which stimulates scientists to find other metallic drugs to replace cisplatin. Iridium (III) complexes, renowned for their favorable attributes such as photostability, high quantum yield, effective cell membrane permeability, extended fluorescence lifetime, and minimal cytotoxicity, have emerged as promising candidates in areas like bioimaging, cellular fluorescent probes, and agents for visualizing biological targets [5–8]. Certain iridium (III) complexes exhibit targeted therapeutic properties, specifically through their ability to accumulate within tumor cells and target mitochondria. This localization triggers an overload of reactive oxygen species and causes changes of mitochondrial membrane potential, ultimately culminating in mitochondrial dysfunction and consequent cell death [9–11]. Recent years have witnessed substantial attention directed towards the potential of iridium (III) complexes, revealing a repertoire of intriguing anticancer activities [12–23]. For instance,

* Corresponding author.
E-mail address: lyjche@gdpu.edu.cn (Y. Liu).

https://doi.org/10.1016/j.ejmech.2024.116295
Received 16 January 2024; Received in revised form 26 February 2024; Accepted 28 February 2024
Available online 29 February 2024

Zhang et al. demonstrated that $[Ir(PPY)_2(DCDPPZ)](PF_6)$ interacts with DNA through minor-groove intercalation, thereby triggering apoptosis in SGC-7901 cells via dysfunction of mitochondria [10]. Similarly, $[Ir(PPY)_2(TFPIP)](PF_6)$, when encapsulated in liposomes, triggers both ROS-mediated apoptosis and GSDME-mediated pyroptosis [24]. Notably, Sobczak-Thépot reported that a half-sandwich iridium (III) complex, IrBDP, efficiently interacts on the mitochondria and the endoplasmic reticulum, leading to cell death [25]. In our previous work, we found the iridium (III) complexes or liposomes entrapped iridium (III) complexes coordinated by the polypyridyl ligands containing one or two chloride atoms or $–NH_2$ show high anticancer efficiency against A549 cells [13,26,27]. In light of pursuit of enhanced insight into anticancer activities and mechanisms, this study introduces a novel polypyridyl ligand simultaneously containing two chloride atoms and one $–NH_2$: 4,6-dichloro-5-(1*H*-imidazo [4,5-f]phenanthroline-2-yl) pyrimidin-2-amine (DPPA). Subsequently, complexes were synthesized: $[Ir(ppy)_2(DPPA)](PF_6)$ (2a) (where ppy denotes deprotonated 2-phenylpyridine), $[Ir(bzq)_2(DPPA)](PF_6)$ (2b) (with bzq representing deprotonated benzo[h]quinoline), and $[Ir(piq)_2(DPPA)](PF_6)$ (2c) (piq indicating deprotonated 1-phenylisoquinoline) (Scheme 1). Detailed investigations for 2a, 2b and 2c were conducted to evaluate the anticancer effects *in vitro* and in vivo.

2. Results and discussion

2.1. Syntheses and characterization

The ligand 4,6-dichloro-5-(1H-imidazo[4,5-f]phenanthroline-2-yl) pyrimidin-2-amine (DPPA) was prepared through refluxing phenanthroline-5,6-diamine with 2-amino-4,6-dichloropyrimidine-5-caraldehyde in ethanol. 2a, 2b, 2c were synthesized by the reaction of $[Ir(ppy)_2Cl]_2{\cdot}H_2O$, $[Ir(bzq)_2Cl]_2{\cdot}H_2O$ or $[Ir(piq)_2Cl]_2{\cdot}H_2O$ with DPPA in CH_2Cl_2 and CH_3OH. The complexes were characterized by ^1H NMR, ^{13}C NMR and HRMS spectra. In the HRMS spectra of the complexes, the determined molecular weights are line with those of calculated values. In the ^{1}HNMR spectra of ligand DPPA, the single signal of proton (14.1 ppm) at the imidazole ring was discovered, whereas in the spectra of 2a, 2b and 2c, this signal was not observed. Owing to coordination of ligand with metal atom, induction of electron deficiency resulted in a very active of NH proton in the imidazole ring. In PBS solution, the UV–Vis and luminescence spectra of 2a, 2b and 2c was determined. As illustrated in Fig. S1a (SI), 2a, 2b, 2c (20.0 μM) exhibit a maximum absorbance at 266 ($\varepsilon = 29350$), 263 ($\varepsilon = 28600$) and 293 nm ($\varepsilon = 31950$). The luminescence of 2a ($\lambda_{ex} = 310$ nm), 2b ($\lambda_{ex} = 305$ nm) and 2c ($\lambda_{ex} = 300$ nm) is depicted in Fig. S1b (SI), the maximum for 2a, 2b, 2c appears at 629, 619 and 609 nm, respectively.

In PBS solution, the stability of 2a, 2b and 2c was examined by UV–Vis spectra, See from Fig. S2 (SI), at 0 and 48 h, no change in the peak shape was observed, which indicated that the complexes are stable in PBS solution in all the cell experiments.

CH_3OH and H_2O as a mobile phase, the purity of 2a, 2b and 2c was measured by HPLC. As depicted in Fig. S3 (SI), the chromatograms exhibited a dominant peak during the 30-min analysis period, with purities of 95.05% for 2a, 96.02% for 2b and 95.67% for 2c.

In all the cell experiments, complexes 2a, 2b and 2c were dissolved in DMSO (final DMSO concentration <0.05%), the complexes were diluted to obtain a series of different concentration of the complexes. During the process of dilution, no precipitate was found.

Table 1
Selected bond lengths [Å] and bond angles [°].

Ir–N1	2.070(5)	Ir–N2	2.069(5)
Ir–N3	2.151(5)	Ir–N4	2.153(4)
Ir–C15	2.025(5)	Ir–C30	2.028(5)
N1–Ir–N3	88.05(19)	N1–Ir–N4	99.14(19)
N2–Ir–N1	171.36(19)	N2–Ir–N3	98.57(19)
N2–Ir–N4	87.79(18)	N3–Ir–N4	77.26(18)
C15–Ir–N1	79.8(2)	C15–Ir–N2	94.1(2)
C15–Ir–N3	94.4(2)	C15–Ir–N4	171.6(2)
C15–Ir–C30	91.4(2)	C30–Ir–N1	94.8(2)
C30–Ir–N2	79.1(2)	C30–Ir–N3	174.00(19)
C30–Ir–N4	97.0(2)		

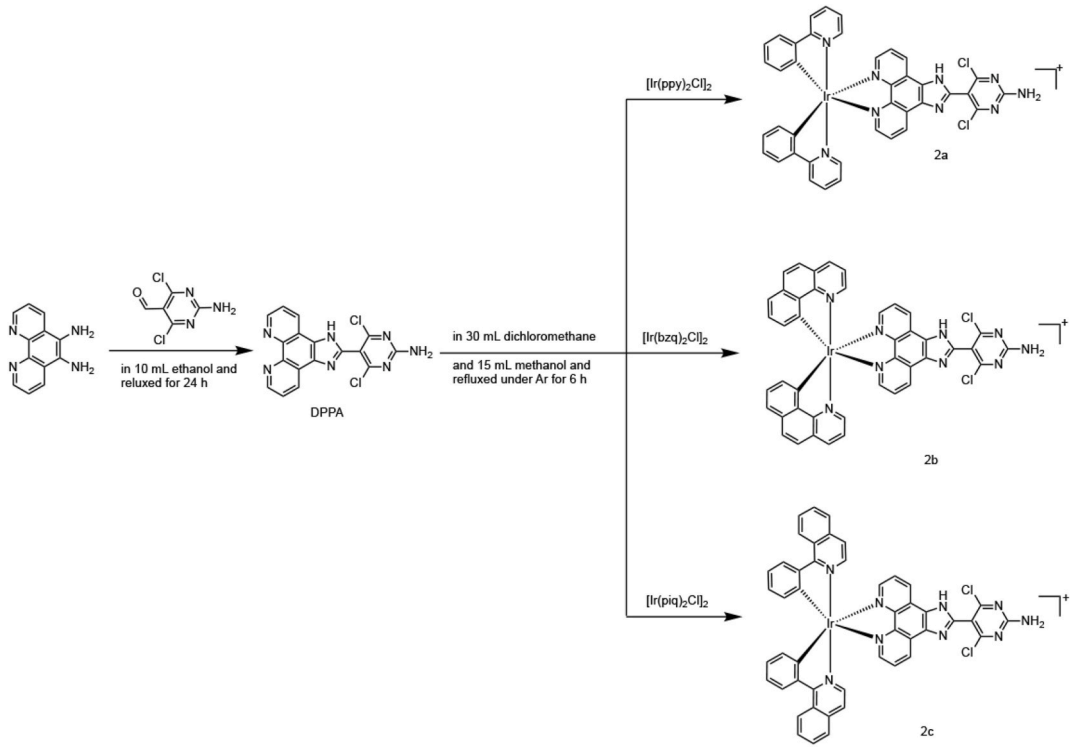

Scheme 1. Synthetic route of DAPP and its complexes 2a, 2b, 2c.

The selected bond lengths and angles are listed in Table 1, the ORTEP diagram for 2c is depicted in Fig. 1, in the crystal structure, no anion PF_6^- was uncovered due to exit of H atom from the imidazole ring, similar results can be discovered in our previous work [28]. While in the ^{19}F NMR spectra of 2c, six fluorine atoms were observed, which further validates that the leaving of H atom in the imidazole ring in the crystal structure of 2c without anion. The Ir atom, a distorted octahedral geometry, is coordinated by ligand DPPA and two ancillary ligands piq. The mean bond lengths of Ir–N and Ir–C are 2.111 and 2.027 Å.

2.2. IC_{50} values determination

The assessment of cellular cytotoxicity was undertaken utilizing the MTT assay (MTT = 3-(4,5-dimethylthiazol-2-yl)-2,5-diphenyltetrazolium bromide) [29] to investigate the impact of DPPA and 2a, 2b, and 2c on cell proliferation. Selected cancer cell lines were exposed to varying concentrations (1.56–100 μM) of ligand DPPA, as well as 2a, 2b, and 2c for a duration of 48 h, with the resulting IC_{50} values summarized in Table 2. Notably, 2a, 2b, and 2c exhibited potent cytotoxic activity against A549, B16, and HCT116 cells. Furthermore, the complexes demonstrated a notably heightened cytotoxic effect compared to the ligand DPPA on the selected cancer cell lines under identical conditions, suggesting a substantial enhancement of cytotoxic activity upon DPPA to form complexes 2a, 2b and 2c. Also, Table 2 illustrates that the cytotoxicity of the complexes on A549, B16, HCT116, HepG2 follow the sequence of 2c > 2b > 2a. This can be explained by the lipid water partition coefficient. The lipid water partition coefficient of 2a, 2b and 2c were measured to be 0.2585, 0.2721 and 0.3609, respectively. Consequently, the cytotoxic activity of 2a, 2b and 2c is line with their lipid water partition coefficient. The cytotoxic potential of the complexes towards A549, B16, and HCT116 cells was found to surpass that of cisplatin, and their cytotoxic activity is higher than iridium(III) complex Ir(ppy)2(BAPIP[Ir(ppy)$_2$(BAPIP)](PF$_6$) (BAPIP = 5-bromo-2-amino-2'-(phenyl-1H-imidazo[4,5-f][1,10]phenanthroline and comparable with liposome-encapsulated iridium (III) complex (IC_{50} = 4.9 ± 1.0 μM for A549, 5.7 ± 0.3 μM for B16) against A549 and B16 [30]. The selectivity indexes of 2a, 2b and 2c of IC_{50} values of LO2 cell versus A549 cell are 9.8, 8.3 and 15.9, respectively. The high SI values indicated that 2a, 2b and 2c have choice on the cancer and non-cancer cells. Given that 2a, 2b, and 2c exhibited the highest cytotoxic efficacy on A549 cells, this cell line was chosen for subsequent anticancer activity studies.

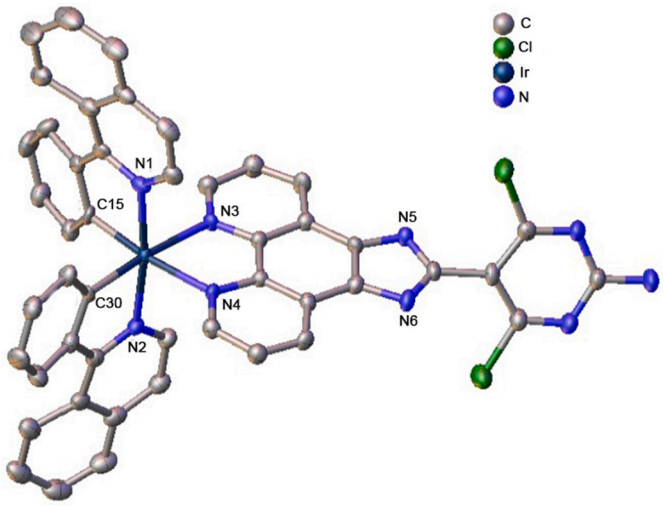

Fig. 1. X-ray crystal structure of **2c** set at a 50% probability. The H atoms, two water and two methanol molecules are omitted for clarity.

Table 2
IC_{50} values (μM) of DPPA and 2a, 2b, 2c towards the selected cancer cells for 48 h.

Complexes	A549	B16	HCT116	HepG2	LO2	SI
DPPA	17.8 ± 1.3	17.6 ± 1.2	18.8 ± 1.8	26.5 ± 4.3	43.7 ± 4.4	2.5
2a	5.6 ± 0.1	8.4 ± 0.8	10.9 ± 0.2	15.0 ± 1.5	54.8 ± 1.9	9.8
2b	3.9 ± 0.3	4.4 ± 1.1	3.7 ± 0.1	11.4 ± 0.7	32.4 ± 1.4	8.3
2c	2.2 ± 0.1	2.5 ± 0.7	2.5 ± 0.1	3.1 ± 0.9	35.0 ± 0.5	15.9
Cisplatin	6.1 ± 0.4	28.8 ± 3.3	15.3 ± 1.2	8.8 ± 1.2	18.4 ± 3.2	3.0

SI Selectivity index of DPPA, 2a, 2b and 2c of IC_{50} values of LO2 cell versus A549 cell.

2.3. Cell colonies and wound healing studies

Malignant tumor cells grow rapidly and infiltratively, invading surrounding tissues and forming indistinct borders. Hence, it is urgent to find new drugs to inhibit cancer cell proliferation and migration. To explore the impact of 2a, 2b and 2c on cell migration and growth, we carried out the cell colonies and wound healing experiments. As depicted in Fig. S4 (SI), A549 cells were subjected to treatment with 2a, 2b, and 2c for 24 h, resulting in a discernible reduction of viable cells. Fig. S5 (SI) further demonstrated an evident increase in wound width relative to the control, indicative of the complexes' pronounced efficacy in hindering both cell colony formation and migration.

2.4. Cellular uptake, co-location, mitochondrial permeability, and the change of mitochondrial membrane potential

A fundamental prerequisite for a drug to exert an anti-cancer effect is its ability to traverse the cellular membrane. Consequently, we initiated our investigation by probing the cellular uptake. As demonstrated in Fig. S6a (SI), following co-incubation of A549 cells with 2a, 2b, and 2c for 12 h, Hoechst 33342 stained cell nuclei blue, while 2a, 2b and 2c exhibited green fluorescence. Merging the images revealed an envelopment of the blue nuclei by the green fluorescence, strongly indicating that 2a, 2b and 2c effectively penetrated the cell and accumulated within the cytoplasm. Given the significance of the endoplasmic reticulum as a hub for cellular synthesis beyond nucleic acids, encompassing proteins, lipids, and sugars, and the pivotal role of mitochondria in furnishing energy for various cellular activities, we proceeded to investigate whether 2a, 2b and 2c localized within the endoplasmic reticulum or mitochondria.

We have quantitatively examined the cellular uptake, the distribution of the complexes in the mitochondria, cell nuclei and cytoplasm using inductively coupled plasma-mass spectrometry (ICP-MS). As listed in Table 3, A549 cells were incubated with 10.0 μM of 2a, 2b and 2c for 4 h, all the uptaken amounts of the complexes 2a, 2b and 2c are 73.47 ± 2.24, 138.45 ± 4.23 and 99.82 ± 3.53 ng/10^6 cells, while the uptaken amounts distributed in the mitochondria are 55.60 ± 2.03 for 2a, 74.01 ± 2.74 for 2b and 75.81 ± 3.12 ng/10^6 cells for 2c, hence, most complexes uptaken by the cells distribute in the mitochondria and cytoplasm, few amounts of the complexes enter the cell nuclei. The cellular uptaken amounts follow the order 2b > 2c > 2a, this is not line with

Table 3
The uptaken amount and the distribution of the complexes in the cells (ng/10^6 cells).

complexes	uptaken amount	mitochondria	nuclei	cytoplasm
2a	73.47 ± 2.24	55.60 ± 2.03	1.07 ± 0.03	6.79 ± 0.24
2b	138.45 ± 4.23	74.01 ± 2.74	1.33 ± 0.04	36.46 ± 1.35
2c	99.82 ± 3.53	75.81 ± 3.12	1.32 ± 0.02	21.48 ± 1.22

those of cytotoxicity of 2c > 2b > 2a, consequently, we consider that the cytotoxic activity is not only closely related to the cellular uptaken amount, but also the nature of the complexes.

As depicted in Figs. S6b and S6c (SI), treatment of A549 cells with 2a, 2b and 2c for 4 h exhibited red staining with ER Tracker Red or Mito-Tracker Red, respectively. The co-localization of the red and green fluorescence signified that 2a, 2b and 2c indeed localized within endoplasmic reticulum and mitochondria. This interaction with the mitochondria, in turn, elicits the opening of the mitochondrial membrane permeability transition pore. To further discern the influence of 2a, 2b and 2c on this transition pore, A549 cells were subjected to incubation with lonomycin (positive control) and 2a, 2b and 2c for 24 h. As revealed in Fig. S6d (SI), the green fluorescence was attenuated in comparison to the control or the negative group, suggesting that the complexes prompt the opening of the mitochondrial permeability transition pore, culminating in mitochondrial dysfunction and a subsequent reduction in mitochondrial membrane potential. This was corroborated by the findings in Fig. S6e (SI), where, under normal conditions, JC-1 emitted vivid red fluorescence, but upon treatment with cccp (a positive control) or 2a, 2b, and 2c for 24 h, the emission shifted to green fluorescence, indicative of decreased mitochondrial membrane potential. To account for potential interference of the green fluorescence emitted by 2a, 2b and 2c, we used 2a, 2b and 2c as references to eliminating the impact of 2a, 2b and 2c on the green fluorescence intensity. Illustrated in Fig. S6f (SI), substantiated that the treatment of A549 cells with cccp or 2a, 2b, and 2c caused a reduction in the ratio of red to green fluorescence relative to the control. Collectively, our observations affirm the complexes' cellular entry and cytoplasmic accumulation, their interaction with the endoplasmic reticulum and mitochondria, resulting in compromised mitochondrial function, the open of the mitochondrial permeability transition pore, and ultimately, a decline in mitochondrial membrane potential.

2.5. Intracellular ROS determination

Reactive oxygen species (ROS) and various apoptotic inducers are known to initiate diverse forms of apoptosis, often accompanied by disruptions in mitochondrial function such as depolarisation and altered membrane potential. Given that the complexes induce an open of the mitochondrial permeability transition pore along with a reduction in mitochondrial membrane potential, it is reasonable to expect consequential changes in the concentration of reactive oxygen species. To gauge intracellular ROS levels, we employed the 2′,7′-dichlorodihydrofluorescein diacetate (DCFH-DA) as non-fluorescent cell-permeant probe. Upon internalization, hydrolysis, and oxidation by a variety of ROS, DCHF-DA is transformed into 2′,7′-dichlorofluorescein (DCF), emitting characteristic green fluorescence. As illustrated in Fig. S7a (SI), minimal green fluorescence was discovered in the control group, whereas upon incubation of A549 cells with Rosup (as a positive control), 2a, 2b, and 2c for 24 h, an enhancement of green fluorescence intensity was uncovered. This starkly indicates that 2a, 2b and 2c significantly elevate intracellular ROS amounts. To preclude the potential influence of the complexes' green fluorescence emission, we used complexes as references to quantitatively measure the green fluorescence intensity. As depicted in Fig. S7b (SI), the green fluorescence intensity increased by 1.89 ± 0.32, 1.42 ± 0.18, 1.47 ± 0.22, and 1.21 ± 0.14 times for Rosup, 2a, 2b, and 2c, respectively, compared to the control. The effect on ROS amounts followed the sequence 2b > 2a > 2c, which diverges from the order of cytotoxic activity of 2a, 2b and 2c towards A549 cells.

2.6. Intracellular Ca^{2+} concentration

Elevation in intracellular calcium ion levels is known to trigger the open of the mitochondrial permeability transition pore, ultimately leading to the release of cytochrome C and initiation of the intrinsic apoptotic pathway [31]. In our examination of intracellular calcium concentration, we employed Fluo-3 AM as a fluorescence probe. Fluo-3 AM is a widely used indicator for Ca^{2+} levels, upon entering the cells, it undergoes cleavage by endogenous esterase to generate Fluo-3, which readily binds with Ca^{2+} to emit green fluorescence. As illustrated in Fig. S8a (SI), co-incubation of A549 cells with 2a, 2b, and 2c for 24 h led to a noticeable increase in green fluorescence, indicating an augmentation in intracellular Ca^{2+} levels. Quantitative analysis (Figs. S8b and SI) further corroborated this finding, demonstrating a 1.99-fold increase for 2a, 1.98-fold increase for 2b, and 2.08-fold increase for 2c in comparison to the control. Collectively, our results strongly suggest that the complexes have the capacity to elevate intracellular Ca^{2+} content.

2.7. Release of cytochrome C

Cytochrome C (cyto C) serves as an essential electron transporter within the mitochondrial respiratory chain. Upon the initiation of apoptosis, specifically through the intrinsic pathway, alterations in mitochondrial membrane permeability result in the release of cyto C into the cytoplasm [32,33]. This translocation of cytochrome C is a pivotal event in activating the mitochondrial signaling pathway during apoptosis. Illustrated in Fig. S9 (SI), the control cells displayed a weak green fluorescence signal, suggesting minimal cytochrome C release. However, when A549 cells were subjected to 2a, 2b, and 2c for 24 h, a conspicuous increase in green fluorescence was observed. This heightened fluorescence is indicative of a notable release of cyto C from the mitochondria into the cytoplasm, substantiating the activation of the intrinsic apoptotic pathway induced by the complexes.

2.8. Impact of the complexes on RNA-sequence

RNA was extracted after A549 cells were incubated with 2c for 24 h. Total RNA was analyzed by RNA-Sequence to further explore the cellular signaling pathway by which 2c hindering the cell proliferation. As shown in Fig. 2a (heat map) and **2b** (volcano map), we found that 2c regulated 151 genes expression, in which 61 and 90 genes were raised and downgraded, respectively. As shown in Fig. 2c, the KEGG enrichment shows that 2c causes cell death through several signaling pathways including calcium ion and ferroptosis. The GO enrichment analysis found that biological process, cellular process, and molecular function were enriched (Fig. 2d).

2.9. Cell cycle distribution, apoptosis, and expression of proteins

The observed impact of the complexes on cell cytotoxicity, colony formation, and wound healing collectively validates their efficacy in restraining cell proliferation and migration. To unravel the potential mechanism responsible for the inhibition of cell growth, a meticulous examination of cell cycle distribution was conducted. The results in Fig. 3a elucidate a noteworthy increase of 4.5% for 2a (II), 8.1% for 2b (III), and 8.7% for 2c (IV) in the S phase, accompanied by corresponding reductions in the G0/G1 and G2/M phases when contrasted with the control (I). This signifies that the complexes exert their inhibitory effect primarily during S phase.

Given that hindrance of cell proliferation often entails cell death or apoptosis, a pivotal programmed process, the impact of 2a, 2b and 2c on apoptosis was further examined using acridine orange. See from Fig. 3b, the living and apoptotic cells were stained green, we observed the apoptotic features of apoptotic cells such as nuclear shrinkage, chromatin condensation. In addition, the apoptotic percentage was determined with flow cytometry, cisplatin was used as a positive control. As presented in Fig. 3c, treatment of A549 cells (I) with 2 × IC_{50} of 2a (IV), 2b (VII), 2c (X) and cisplatin (XII) for 24 h resulted in a substantial rise of 4.56%, 10.59%, 9.19% and 3.38%, respectively, in early apoptotic cells when compared to the control. However, A549 cells were incubated with 2 × IC_{50} of 2a (IV), 2b (VII), 2c (X) and cisplatin (XII) for 48 h

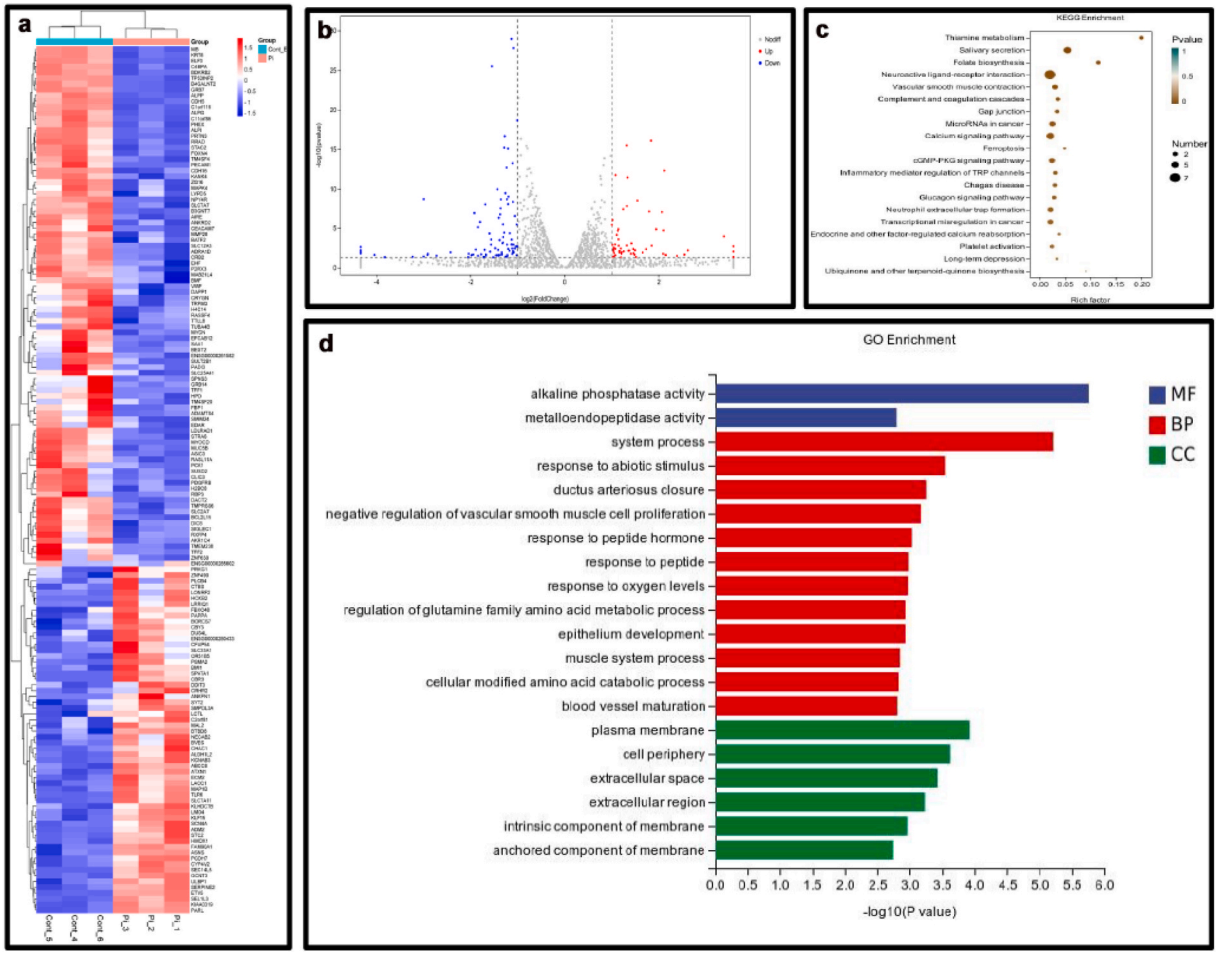

Fig. 2. RNA-sequence determination (a) Heap map, (b) volcano map, (c) and (d) KEGG and GO enrichment.

(Fig. 3d), the apoptotic percentage increased by 13.24% for 2a, 14.84% for 2b and 79.64% for cisplatin in the late apoptosis, while 2c caused an increase of 67.98% in the early apoptosis. Therefore, we conclude that 0.5 × IC_{50} or IC_{50} concentration of 2a, 2b and 2c show low or no apoptotic effect, 48h-treatement displayed a high apoptotic efficacy than that of 24h-treatment, 2a, 2b and cisplatin induce a late apoptosis, while 2c causes an early apoptosis. The late apoptotic effect of 2a and 2b is lower than that of cisplatin, the early apoptotic efficacy of 2c is higher than cisplatin after a treatment of 48 h.

The expression of Bax, PARP (poly ADP-ribose polymerase), caspase 3 and Bcl-2 was investigated by Western blot. It's noteworthy that the cleavage of PARP serves as a hallmark of apoptosis initiated by caspase activity. Additionally, Bcl-2 family proteins, encompassing pro-apoptotic Bax and anti-apoptotic Bcl-2, are pivotal in the orchestration of cellular apoptosis [34,35]. This intricate interplay becomes apparent in Fig. 3e, wherein co-incubation of A549 cells with 2a, 2b, and 2c for 24 h leads to a downregulation of PARP, caspase 3, and Bcl-2, alongside an increase in Bax protein expression. Taken together, we consider that 2a, 2b and 2c orchestrate apoptosis through caspase 3 activation, PARP cleavage, and modulation of Bcl-2 family protein expression.

2.10. *Complexes inducing ferroptosis*

Distinguished by its distinct iron-dependent nature and different from autophagy, necrosis, and apoptosis, ferroptosis is an emerging form of cell death. The increase in ROS is intricately linked with both apoptosis and ferroptosis. Central to the regulation of lipid peroxidation is glutathione peroxidase 4 (GPX4), which plays a pivotal role in suppressing it by preventing the depletion of glutathione (GSH), ultimately thwarting ferroptosis [36,37]. The depletion of GSH occurs through its reaction with lipid ROS, resulting in the production of glutathione disulfide (GSSG). As displayed in Fig. 4a, a discernible reduction in GSH content is observed in A549 cells treated with complexes 2a, 2b, and 2c when compared to the control, illustrating the effective reduction of GSH content by the complexes.

Lipid peroxidation, as evidenced by malondialdehyde (MDA) levels, was subsequently assessed to further explore the influence of 2a, 2b, and 2c on cellular lipid peroxidation. As demonstrated in Fig. 4b, treatment of A549 cells with 2a, 2b and 2c for 24 h led to a notable increase in MDA levels when contrasted with the control, signifying their impact on lipid peroxidation. Inhibition of GPX4 activity is recognized to prompt intracellular lipid peroxidation, a pivotal marker of ferroptosis. This is corroborated in Fig. 4c, where the expression of GPX4 was downregulated in response to treatment of A549 cells with 2a, 2b, and 2c.

Assessment of lipid peroxidation was further facilitated using 4,4-difluoro-5-(4-phenyl-1,3-butadenyl)-4-bora-3a,4a-diaza-sindacene-3-undecanoic acid (C11-BODIPY) as a fluorescent marker. This fluorescent marker dichotomously represents low and high degrees of lipid peroxidation through red and green fluorescence, respectively [38,39]. As presented in Fig. 4d and e, the control group displayed red fluorescence, indicative of a low degree of lipid peroxidation, whereas the groups treated with 2a, 2b, and 2c exhibited bright green fluorescence, signifying a high degree of lipid peroxidation. Collectively, these results illuminate that 2a, 2b, and 2c induce lipid peroxidation and consequently invoke ferroptosis, providing a comprehensive understanding of the mechanisms underpinning their cellular impact. These results show

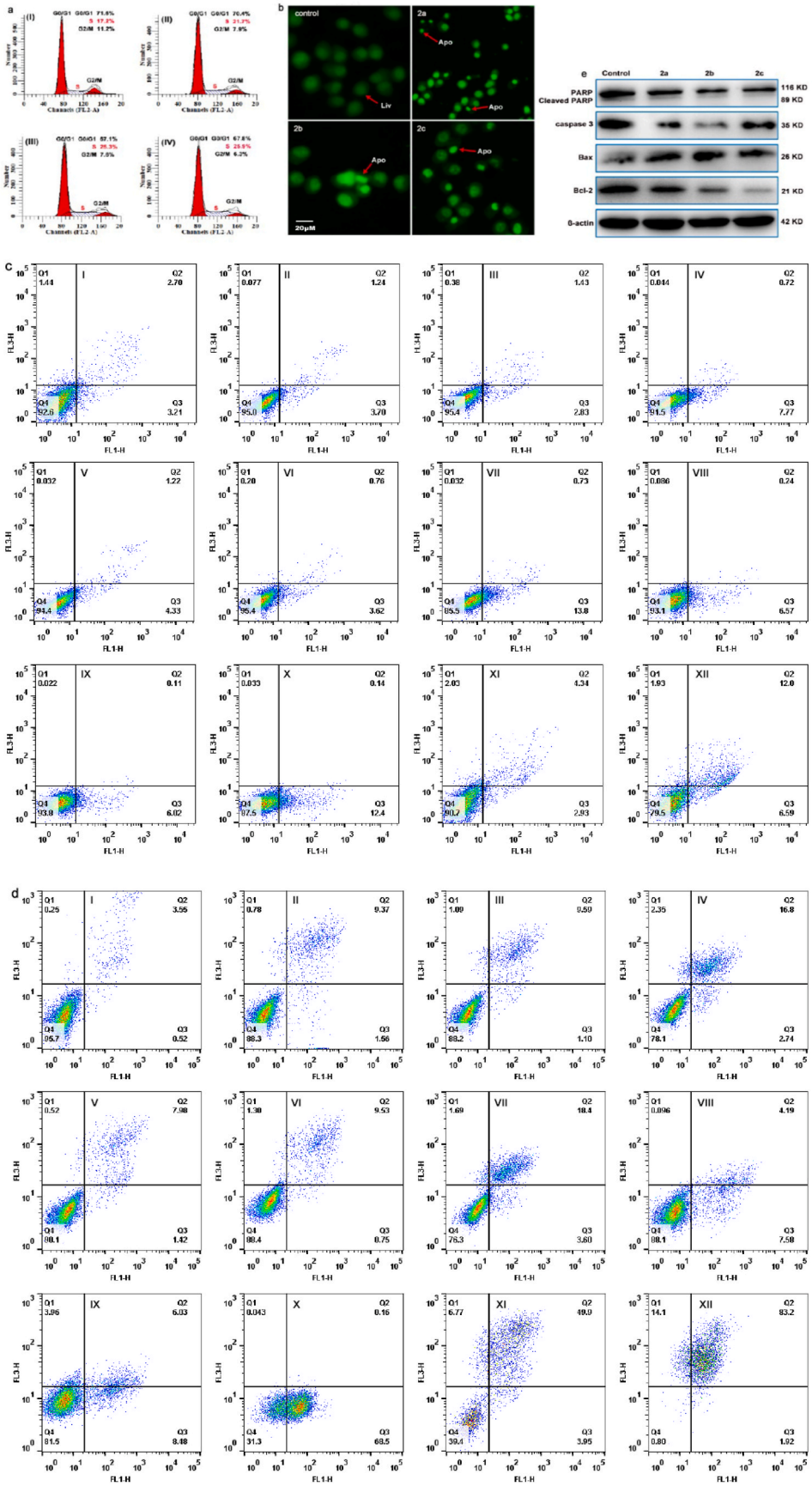

Fig. 3. (a) cell cycle distribution, (b) morphological apoptosis, (c) and (d) apoptosis after A549 cells (I) were exposed to 0.5 × IC_{50}, IC_{50} and 2 × IC_{50} concentrations of 2a (II-IV), 2b (V-VII), 2c (VIII-X) and IC_{50} and 2 × IC_{50} concentrations of cisplatin (XI-XII) for 24 or 48 h.

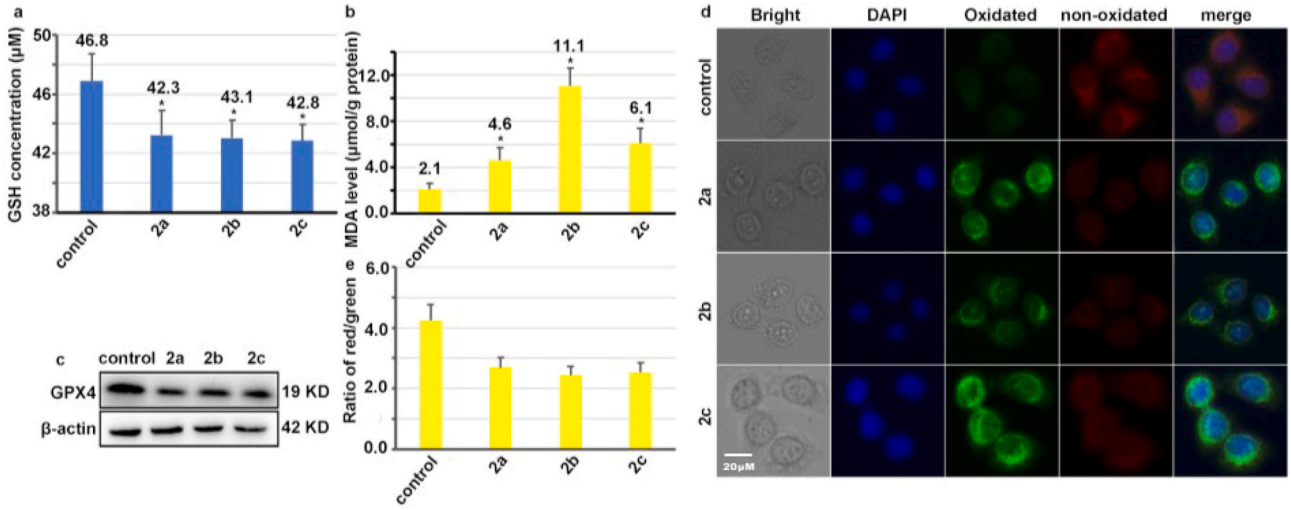

Fig. 4. (a) GSH, (b) MDA concentration determination, (c) the expression of GPX4, (d) lipid peroxidation detection while A549 cells were stained with C11-BODIPY$^{581/591}$, (e) Ratio of red versus green fluorescence.

that the complexes can cause ferroptosis.

2.11. Induction of pyroptosis

Programmed cell death is an orchestrated process triggered by specific signals or stimuli, ensuring the preservation of the internal cellular environment. Among the diverse forms of programmed cell death, cellular pyroptosis is notable. To probe the impact of the complexes on pyroptosis, an examination of cell morphology was carried out. In Fig. 5a, co-incubation of A549 cells with 2a, 2b, and 2c for 28 h revealed characteristic membrane bubbles on the plasma membrane. This phenomenon arises due to the breach of the cell membrane and subsequent cellular swelling driven by osmotic pressure disparities between the cell interior and its surroundings, signifying the ability of 2a, 2b, and 2c to induce pyroptosis.

Lactate dehydrogenase (LDH) release serves as a direct indicator of pyroptosis. As illustrated in Fig. 5b, treatment of A549 cells with 2a, 2b, or 2c resulted in elevated LDH content compared to the control, providing further evidence of the pyroptotic effect induced by these complexes.

The molecular underpinnings of cellular pyroptosis encompass two key pathways, one of which is reliant on the classical caspase 1 pathway. In the context of innate immune response, pathogenic invasion triggers the formation of inflammasome complexes that activate caspase 1. Activated caspase 1 serves a dual role: it cleaves Gasdermin D to yield a peptide harboring the N-terminal reactive domain of Gasdermin D, inducing cell membrane perforation, cellular rupture, and the subsequent release of cellular contents, culminating in an inflammatory response. As shown in Fig. 5c, the complexes cleave GSDMD-F into GSDMD-N, downregulate caspase 1, upregulate the expression of NF-kB protein. Collectively, 2a, 2b and 2c can trigger pyroptosis.

2.12. Antitumor effect in vivo

Given that 2c exhibited the most potent anticancer efficacy on A549 cells, thus, 2c was chosen for further in vivo antitumor investigations. The initial step was to determine the LD50 value through acute toxicity assessment. As depicted in Fig. 6a and b, the administration of 60, 90, and 120 mg/kg doses of 2c to Kunming mice led to noticeable reductions in body weight and instances of mice mortality. However, no significant alterations in body weight and no mouse deaths were uncovered in the 30 or 40 mg/kg doses of 2c. Therefore, LD50 value was 64 mg/kg after 14 days of treatment.

For the subsequent in vivo antitumor study, athymic BALB/c nude mice were allocated into three groups ($n = 6$): control, 3.2, and 5.0 mg/kg of 2c. The mice were treated with the respective doses of 2c, and their body weights and tumor volumes were monitored daily. Upon completion of the 8-day treatment, the nude mice were euthanized, then the tumors were collected. Fig. 6c, d, and 6e illustrate that the tumor size and weight in the 2c groups are notably diminished compared to the control group. The tumor inhibitory rate reached 34.04% and 58.58% for the 3.2 mg/kg and 5.0 mg/kg of 2c, respectively (Fig. 6f). The inhibitory rate of 2c is lower than liposome-entrapped iridium(III) complex [Ir(ppy)$_2$(DAPIP)](PF$_6$) (inhibitory rate of 70.4%) [30].

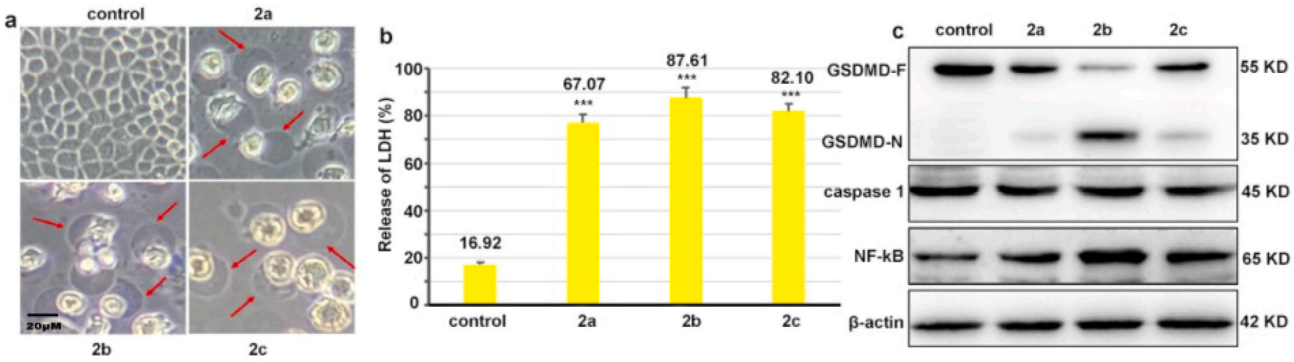

Fig. 5. Pyroptosis assay (a) cell morphology, (b) LDH release, (c) expression of GSDMD, caspase 1, NF-kB.

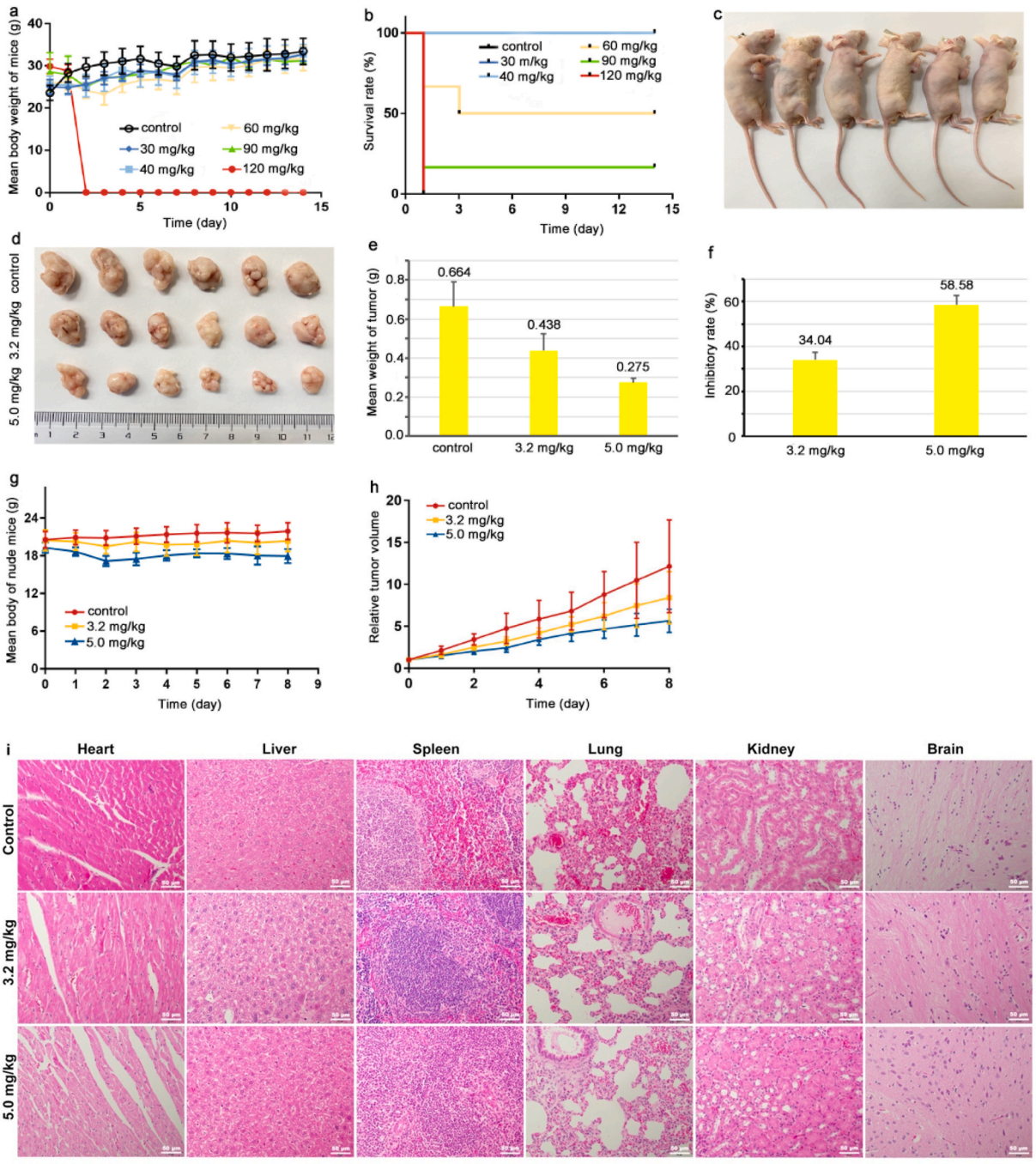

Fig. 6. In vivo antitumor (a) mean body weight of kunming mice, (b) survival rate of Kunming mice, (c, d and e) Photographs of tumor size and weight from treatment and vehicle groups, (f) Inhibitory rate of 3.2 mg/kg and 5.0 mg/kg of 2c, (g) Body weight of the nude mice and (h) relative tumor volumes after the tumors were treated with 2c for 8 days, (i) Histopathological sections using H&E staining.

Importantly, as demonstrated in Fig. 6g, in the body weights of the mice, there were no discernible alterations between the control and 2c groups. The relative tumor volumes displayed a decrease in the 2c groups comparison to the control (Fig. 6h). Additionally, histological examination of various tissues including heart, liver, lung, spleen, kidney, and brain using Hematoxylin-Eosin (H&E) staining revealed no significant deviations in heart, spleen, kidney, brain and liver tissue, only observing a mild edema and the presence of bruising in the lungs (Fig. 6i). Taken together, these findings underscore the potent antitumor efficacy of 2c in vivo and its favorable safety profile in key organs.

3. Conclusions

In conclusion, this study successfully synthesised and comprehensively characterised three iridium (III) complexes, namely 2a, 2b, and 2c. The complexes enter the cells and mainly distribute in the mitochondria and cytoplasm. Notably, these complexes demonstrated significant cytotoxic activity against A549, B16, and HCT116 cancer cells. Moreover, they effectively hindered cell colonies and cell migration. Further exploration of their impact on cell cycle distribution indicated that the complexes exerted their anti-proliferative effects by arresting A549 cells at the S phase. Additionally, 2a, 2b and 2c were found to elicit intricate changes within the cells. Specifically, they heightened

intracellular amount of ROS, triggered a reduction in mitochondrial membrane potential and induced augmented intracellular calcium ion content, culminating in the release of cytochrome *c*. RNA-sequence analyses underscored the comprehensive impact of complex 2c on gene expression, revealing a significant modulation of 61 upregulated and 90 downregulated genes. KEGG enrichment analysis shed light on the pathways including calcium ions and ferroptosis as pivotal players in the induction of cell death. The downregulation of GPX4 expression, a reduction of glutathione (GSH) concentration, an elevation in malondialdehyde (MDA) levels and C11-BODIPY$^{581/591}$ dyed experiments show that the complexes can induce ferroptosis. The finding of characteristic membrane bubbles, cleavage of GSDMD-F into GSDMD-N, downregulation of caspase 1, upregulation of the expression of NF-kB protein and LDH release indicate that the complexes can cause pyroptosis. The in vivo antitumor assessments further accentuated the potential of complex 2c, showcasing remarkable antitumor efficacy (58.58%) without adverse effects on critical organs. Complex 2c cause an early apoptosis, 2a and 2b induce a late apoptosis. The collective evidence suggests that the complexes induce cell death via apoptosis, ferroptosis and GSDMD-mediated pyroptosis. This work provides valuable insights for both understanding the anticancer properties of these iridium (III) complexes and guiding the design and synthesis of novel iridium-based anticancer agents.

4. Experimental

4.1. Materials and method

Starting with the acquisition of essential reagents, $IrCl_3{\cdot}3H_2O$ was procured from J&K Scientific, while Aladdin supplied 1,10-phenanthroline and DMSO. Additionally, Equation Biotechnology Co., Ltd. provided 4′,6-diamidino-2-phenylindole (DAPI). Complementary reagents for the study encompassed 1-phenylpyridine (ppy), 1-phenylisoquinoline (piq), and benzo[h]quinolone (bzq), which were acquired from Beijing HWRK Chem Co., Ltd. The iridium dimeric precursors *cis*-$[Ir(ppy)_2Cl]_2$, $[Ir(bzq)_2Cl]_2$ and $[Ir(piq)_2Cl]_2$ were synthesized according to the methods described as the literature [40].

With dimethyl sulfoxide as the solvent and tetramethylsilane (TMS) as an internal standard, NMR spectra were conducted utilizing a Varian-500 spectrometer (500 MHz). Luminescence and UV–Vis spectra measurements were also executed. The molecular weights of the complexes were meticulously determined employing High Resolution Mass Spectrometry (HRMS).

4.2. Synthesis of DPPA and 2a, 2b and 2c

4.2.1. Preparation of DPPA

A solution consisting of 0.198 g of 2-amino-4,6-dichloropyrimidine-5-carbaldehyde (1.0 mmol) and 0.21 g of 1,10-phenanthroline-5,6-dione (1.0 mmol) was meticulously dissolved in 25 mL CH_3CH_2OH and refluxed at 80 °C for a duration of 24 h. Upon completion of the reflux process, and following cooling to ambient temperature, the solvent was carefully removed. A brown-colored powder was subsequently obtained. The resulting yield amounted to 82%. Anal. Cacld for $C_{17}H_9Cl_2N_7$: C, 53.42, H, 2.37, N, 25.65%. Found: C, 53.18, H, 2.51, N, 25.80%. ^{1}HNMR (DMSO-d_6, 500 MHz): 14.1 (s, 1H), 9.05 (d, J = 5.5 Hz, 1H), 8.88 (d, J = 8.5 Hz, 1H), 8.76 (d, J = 8.0 Hz, 1H), 8.08 (s, 1H), 7.87–7.76 (m, 2H), 6.48 (s, 2H). ^{13}C NMR (DMSO-d_6, 125 MHz): 162.66, 161.71, 148.73, 148.52, 147.84, 144.37, 144.01, 143.98, 135.76, 130.29, 130.12, 126.48, 124.57, 124.11, 123.89, 120.30, 119.64. HRMS (CH_3OH): m/z = 381.9126 ([M − 1]).

4.2.2. Synthesis of 2a, 2b and 2c

A combination of *cis*-$[Ir(ppy)_2Cl]_2$ (0.215 g, 0.20 mmol) [40] for 2a, $[Ir(bzq)_2Cl]_2$ (0.234 g, 0.20 mmol) [40] for 2b, $[Ir(piq)_2Cl]_2$ (0.255 g, 0.20 mmol) [40] for 2c and DPPA (0.152 g, 0.40 mmol) was meticulously dissolved in 28 mL CH_2Cl_2 and 14 mL CH_3OH and refluxed at 40 °C for a period of 6 h under an argon atmosphere. Then the solution was allowed to cool, subsequently, saturated aqueous NH_4PF_6 was added and stirred for 2 h, yielding a distinctive yellow precipitate. The obtained crude product underwent purification via neutral alumina column chromatography, utilizing CH_2Cl_2-acetone (v/v, 5:1) as the eluting agent, the yellow band fraction was collected, finally the yellow powder was attained through removing the solvent.

2a, yield: 80%. ^{1}H NMR (DMSO-d_6, 500 MHz) (Figs. S10 and SI): δ 9.01 (d, J = 8.0 Hz, 2H), 8.24 (d, J = 8.0 Hz, 2H), 8.12–8.09 (m, 1H), 8.00 (d, J = 5.0 Hz, 2H), 7.94 (d, J = 8.0 Hz, 2H), 7.91–7.84 (m, 4H), 7.72 (s, 1H), 7.51 (d, J = 6.5 Hz, 2H), 7.04 (t, J = 7.5 Hz, 2H), 7.00–6.92 (m, 4H), 6.31 (d, J = 7.5 Hz, 2H). ^{13}C NMR (DMSO-d_6, 125 MHz) (Figs. S11 and SI): 172.66, 167.43, 167.33, 162.05, 161.58, 151.68, 151.05, 149.64, 149.48, 148.33, 146.69, 144.55, 144.22, 143.42, 139.07, 138.94, 132.59, 132.13, 131.76, 130.62, 127.32, 126.46, 125.46, 124.26, 122.76, 122.62, 120.35. IR (KBr, cm^{-1}): 3406, 2974, 1639, 1477, 1420, 1350, 1267, 1163, 1064, 1031, 820, 757, 557. ^{19}F NMR (DMSO-d_6, 500 MHz): 69.38 (3F), −70.90 (3F). HRMS (CH_3CN): $C_{39}H_{25}N_9Cl_2IrPF_6$: m/z = 882.12145 [(M − PF_6)$^+$].

2b, yield: 77%. ^{1}H NMR (DMSO-d_6, 500 MHz) (Figs. S12 and SI): δ 8.98 (d, J = 7.5 Hz, 2H), 8.50 (d, J = 7.0 Hz, 2H), 8.08 (t, J = 4.0, 1H), 8.01–7.97 (m 6H), 7.87 (d, J = 9.0 Hz, 2H), 7.81–7.79 (m, 2H), 7.71 (s, 1H), 7.57 (d, J = 8.0 Hz, 2H), 7.45–7.42 (m, 2H), 7.21 (t, J = 7.5 Hz, 2H), 6.34 (d, J = 7.5 Hz, 2H). ^{13}C NMR (DMSO-d_6, 125 MHz) (Figs. S13 and SI): 172.59, 167.99, 162.05, 161.58, 157.01, 156.88, 149.19, 148.49, 147.87, 147.17, 143.86, 140.93, 140.87, 137.93, 137.82, 134.19, 132.59, 132.17, 130.15, 129.92, 129.06, 127.31, 127.11, 126.46, 124.66, 123.22, 120.76, 120.62. IR (KBr, cm^{-1}): 3407, 3032, 1635, 1445, 1404, 1328, 1137, 1070, 1049, 851, 753, 557. ^{19}F NMR (DMSO-d_6, 500 MHz): 69.38 (3F), −70.90 (3F). HRMS (CH_3CN): $C_{43}H_{25}N_9Cl_2IrPF_6$: m/z = 930.12256 [(M − PF_6)$^+$].

2c, yield: 75%. ^{1}H NMR (DMSO-d_6, 500 MHz) (Figs. S14 and SI): δ 9.00 (d, J = 7.5 Hz, 4H), 8.39 (d, J = 8.0 Hz, 2H), 7.99 (dd, J = 2.0, J = 7.5 Hz, 4H), 7.88–7.84 (m, 8H), 7.43–7.39 (m, 4H), 7.16 (t, J = 7.5 Hz, 2H), 6.94 (t, J = 7.5 Hz, 2H), 6.32 (d, J = 8.0 Hz, 2H). ^{13}C NMR (DMSO-d_6, 125 MHz) (Figs. S15 and SI): 172.54, 168.32, 162.19, 161.56, 154.90, 154.41, 145.86, 141.43, 141.26, 136.95, 132.74, 132.42, 132.19, 131.04, 130.95, 130.43, 129.78, 128.15, 126.89, 126.01, 122.78, 122.66. IR (KBr, cm^{-1}): 3410, 2992, 1636, 1504, 1455, 1404, 1385, 1271, 1149, 1133, 1080, 1048, 845, 756, 556. ^{19}F NMR (DMSO-d_6, 500 MHz): 69.39 (3F), 70.90 (3F). HRMS (CH_3CN): $C_{47}H_{29}N_9Cl_2IrPF_6$: m/z = 982.15472 [(M − PF_6)$^+$].

4.3. Detection of purity of 2a, 2b and 2c

The purity of 2a, 2b and 2c was carried out with COSMOSIL 5C_{18}-MS-II column (250 mm × 10 mm) at 25 °C. Mobile phase A consisted of 0.1% trifluoroacetic acid (TFA) with H_2O, mobile phase B was made of 0.1% TFA with methanol, the flow rate reached 3 mL/min. The volume ratios of V_{CH3OH}:V_{H2O} were 90:10 for 2a, 95:5 for 2b, 95:5 for 2c, the detected wavelengths were 254 nm for 2a, 210 nm for 2b and 2c.

4.4. Determination and refinement of crystal structure 2c

Suitable for X-ray diffraction analysis, single crystal of 2c, was grown via slow evaporation of 2c methanol solution (CCDC 2293711) and Table 4 listed the crystal data for 2c. A SuperNova, Dual, Cu at home/near, AtlasS2 diffractometer in the range 3.654 < θ < 73.003° with CuKα radiation (λ = 1.54184 Å) at 150 K was used to measure the crystal structure of 2c. Direct method was applied to solve the structure of 2c to obtain the position of all non-H atoms. All calculation was achieved applying the SHELXTL-97 system [41].

Table 4
Crystal data of $2c{\cdot}2H_2O{\cdot}2CH_3OH$.

	$C_{49}H_{40}Cl_2N_9Ir$
M_r	1082.09
T [K]	150(2)
λ [Å]	1.54184
Crystal system	Monoclinic
Space group	P21/n
a [Å]	10.0777(2)
b [Å]	12.7179(3)
c [Å]	18.3379(5)
α [°]	81.834(2)
β [°]	80.622(2)
γ [°]	72.910(2)
V [Å^3]	2205.43(2)
Z	2
D_c [g·m^{-3}]	1.629
Crystal size [mm]	0.21 × 0.19 × 0.12
θ range for data collection[°]	3.654 to 73.003
Limiting indices, *hkl*	$-8 \le h \le 12$, $-13 \le k \le 15$, $-20 \le l \le 22$
Reflections collected	16070
Independent reflections (R_{int})	8480
Goodness-of-fit on F^2	1.015
R_1/wR_2 [$I > 2\sigma(I)$] [a]	0.0528/0.1203
R_1/wR_2 (all data) [a]	0.0639/0.1262
Largest diff. peak and hole [e Å^{-3}]	2.040 and −1.457

4.5. Cell viability and IC_{50} values determination

Cytotoxic activity assessment against cell lines of human lung carcinoma A549, melanoma B16, colorectal cancer HCT116, human hepatocellular carcinoma HepG2 and non-cancer cell LO2 was conducted using the 3-(4,5-dimethylthiazol-2-yl)-2,5-diphenyltetrazolium bromide (MTT) method [29]. In this approach, cells were seeded into 96-well microassay culture plates at a density of 5×10^3 cells per well and allowed to grow overnight at 37 °C within a 5% CO_2 incubator. Following the initial incubation, varying concentrations of the complexes and ligands were introduced into the wells. The control wells were supplemented with 100 μL of culture medium. The plates were subsequently co-incubated for 48 h. After the incubation period, a stock solution of MTT dye (25 μL, 4 mg mL^{-1}) was introduced into each well. Following an additional 4-h treatment, MTT formazan crystals were dissolved by a solution (100 μL) of DMSO (50%) and sodium dodecyl sulfate (20%). A microplate spectrophotometer was applied to measure the optical density at 490 nm.

4.6. Cellular uptake studies

Seeded in a 12-well plate of A549 at a density of 1.5×10^5 cells per well overnight, 2a, 2b and 2c were added in the above cells for 12 h at 37 °C. Then, the plate was washed three times with PBS buffers to eliminate the residual complexes, and the cells were further dyed with Hoechst 33324 for 20 min. After that, the cells were washed twice with ice-cold PBS, the residual Hoechst was eliminated, ultimately, the cells were photographed.

4.7. Cellular apoptosis studies

Seeded in the six-well plates overnight, A549 cells were incubated with IC_{50} concentrations of 2a, 2b and 2c for 24 h, then A549 cells were harvested, washed three times with PBS. The cells were dyed with 50 μg mL^{-1} PI (propidium iodide) and 1 mg mL^{-1} Annexin V-FITC in PBS on ice in the dark for 15 min. Finally, the cells were analyzed using flow cytometry.

4.8. Cell cycle arrest assay

In this experimental approach, 2×10^5 A549 cells were meticulously seeded in individual wells of 6-well plates and cultured in a medium (10% fetal bovine serum, FBS) overnight. The cells were treated with IC_{50} concentrations of 2a, 2b and 2c for 24 h. The cells were washed twice with PBS and separated using trypsin-EDTA solution. The collected cells were centrifuged to eliminate the supernatant and washed twice with cold PBS, and fixed with 75% ethanol overnight in a refrigerator. Next day, the cells were centrifuged to eliminate the supernatant and washed twice with cold PBS. A mixture of RNAse (30 μL, 10 mg mL^{-1}) and propidium iodide (30 μL, 1.0 mg mL^{-1}), Tritonx-100 (10 μL) and PBS were added to the cells and incubated at 37 °C for 30 min, the cells were analyzed using a FACS Calibur flow cytometer.

4.9. Examination of cell morphology and lactate dehydrogenase (LDH) content

Seeded in a 6-well plate overnight, A549 cells were then treated with 2a, 2b and 2c for 28 h. Afterwards, the cell morphology was carefully observed under an inverted light microscope.

For LDH release studies, cells cultured in a 96-well plate were co-incubated with 2a, 2b and 2c for a period of 24 h. After this treatment, LDH release solution was added to the control group for an hour. Thereafter, the supernatant was transferred to new wells and mixed with LDH detection working solution at 25 °C for 30 min, with precautions taken to avoid light. The absorbance was measured at 490 nm.

4.10. Acute toxicity

Given the relatively low IC_{50} value of the complex 2c on A549 cells, 2c was selected for in vivo antitumor experiments. A half of male and female Kunming mice (KM mice) of 5–6 weeks of age, with body weight range of 20–30 g, were selected and kept in SPF barrier environment. Then they were divided into 6 groups ($n = 6$). The mice were fasted for 12 h before administration, the control group was injected with saline intraperitoneally, different concentration (30, 40, 60, 90, 120 mg/kg) of 2c was injected in the 2c-treated groups, the mice were continuously observed for 14 days, and the weights of the Kunming mice were measured daily. On the 14th day, the mice were executed. The survival rate (%) = ($N_{\text{number of surviving mice}}/N_{\text{total number of mice tested}}$) × 100%. The experimental data recorded daily were compiled and analyzed on Excel software, and finally the LD50 value of complex 2c was gained by SPSS software.

4.11. Antitumor activity in vivo

Complex 2c emerged as the candidate for in vivo antitumor evaluation, all the experimental procedures were authorized by Institutional Animal Center of Guangdong Pharmaceutical University. Guangdong Provincial Laboratory Animal Center provides BALB/c nude mice (3–4 weeks). The mice were injected with a total of A549 (6×10^6/μL), subsequently distributing them into randomized groups: the control group and the positive group. Intraperitoneal injections of 2c (3.2 or 5.0 mg/kg) were administered daily. The mice's body weights and the diameters of tumors were documented daily. The mice were humanely euthanized on the 8th day, and the tumors were meticulously collected and weighed.

4.12. Data analysis

All data was obtained as means ± standard error and the difference was evaluated using student's-test. Differences are significant at $^*P < 0.05$, $^{**}P < 0.01$, $^{***}P < 0.001$. At least three independent experiments were performed.

Note: The procedures for cell culture, lipid water partition coefficient, wound healing experiment, cell colonies formation, co-location, intracellular ROS concentration determination, GSH content determination, intracellular MDA concentration, change of the mitochondrial membrane potential, intracellular Ca^{2+} levels determination, release of

cytochrome c, RNA-sequence assay, protein expression assay can be found in the supporting information.

CRediT authorship contribution statement

Huiyan Hu: Writing – original draft, Methodology, Investigation. **Fan Zhang:** Formal analysis, Data curation. **Zhujun Sheng:** Software. **Shuang Tian:** Data curation. **Gechang Li:** Formal analysis. **Shuanghui Tang:** Software. **Yajie Niu:** Formal analysis. **Jiawan Yang:** Visualization, Software. **Yunjun Liu:** Writing – review & editing, Supervision, Project administration, Conceptualization.

Declaration of competing interest

Authors declare no competing interests exist.

Data availability

Data will be made available on request.

Acknowledgements

We are grateful for National Natural Science Foundation of China (No 21877018).

Appendix A. Supplementary data

Supplementary data to this article can be found online at https://doi.org/10.1016/j.ejmech.2024.116295.

References

[1] B. Vogelstein, K.W. Kinzler, Cancer genes and pathways they control, Nat. Med. 10 (2004) 789–799.
[2] D. Hanahan, R.A. Weinberg, Hallmarks of cancer: the next generation, Cell 144 (2011) 646–674.
[3] K.C. Oeffinger, S.S. Baxi, D.N. Friedman, C.S. Moskowitz, Solid tumor second primary neoplasms: who is at risk, what can we do? Semin. Oncol. 40 (2013) 676–689.
[4] J.Q. Wang, P.Y. Zhang, C. Qian, X.J. Hou, L.N. Ji, H. Chao, Mitochondria are the primary target in the induction of apoptosis by chiral ruthenium(II) polypyridyl complexes in cancer cells, J. Biol. Inorg. Chem. 19 (2014) 335–348.
[5] K.K.W. Lo, Luminescent rhenium (I) and iridium (III) polypyridine complexes as biological probes, imaging reagents, and photocytotoxic agents, Acc. Chem. Res. 48 (2015) 2985–2995.
[6] H.D. Shi, Y. Wang, S.M. Lin, J.X. Lou, Q.L. Zhang, Recent development and application of cyclometalated iridium (III) complexes as chemical and biological probes, Dalton Trans. 50 (2021) 6410–6417.
[7] H.Y. Huang, S. Banerjee, K.Q. Qiu, P.Y. Zhang, O. Blacque, H. Malcomson, M. J. Paterson, G.Y. Clarkson, M. Staniforth, V.G. Stavros, G. Gasser, H. Chao, P. J. Sadler, Targeted photoredox catalysis in cancer cells, Nat. Chem. 11 (2019) 1041–1048.
[8] C. Zhang, K.Q. Qiu, C.F. Liu, H.Y. Huang, T.W. Rees, L.N. Ji, Q.L. Zhang, H. Chao, Tracking mitochondrial dynamics during apoptosis with phosphorescent fluorinated iridium (III) complexes, Dalton Trans. 47 (2018) 12907–12913.
[9] B.B. Chen, N.L. Pan, J.X. Liao, M.Y. Huang, D.C. Jiang, J.J. Wang, H.J. Qiu, J. X. Chen, L. Li, J. Sun, Cyclometalated iridium (III) complexes as mitochondria-targeted anticancer and antibacterial agents to induce both autophagy and apoptosis, J. Inorg. Biochem. 219 (2021) 111450.
[10] Y. Chen, T.W. Rees, L.N. Ji, H. Chao, Mitochondrial dynamics tracking with iridium (III) complexes, Curr. Opin. Chem. Biol. 43 (2018) 51–57.
[11] X.D. Song, X. Kong, S.F. He, J.X. Chen, J. Sun, B.B. Chen, J.W. Zhao, Z.W. Mao, Cyclometalated iridium (III)-guanidinium complexes as mitochondria-targeted anticancer agents, Eur. J. Med. Chem. 138 (2017) 246–254.
[12] Y.C. Chen, Y.Y. Gu, H.Y. Hu, H.M. Liu, W.L. Li, C.X. Huang, J. Chen, L.J. Liang, Y. J. Liu, Design, synthesis and biological evaluation of liposome entrapped iridium (III) complexes toward SGC-7901 cells, J. Inorg. Biochem. 241 (2023) 112134.
[13] H.W. Zhang, L. Tian, R.X. Xiao, Y. Zhou, Y.Y. Zhang, J. Hao, Y.J. Liu, J.P. Wang, Anticancer effect evaluation in vitro and in vivo of iridium(III) polypyridyl complexes targeting DNA and mitochondria, Bioorg. Chem. 115 (2021) 105290.
[14] L.L. Wang, R.L. Guan, L.N. Xie, X.X. Liao, K. Xiong, T.W. Rees, Y. Chen, L.N. Ji, H. Chao, An ER-targeting iridium(III) complex that induces immunogenic cell death in non-small-cell lung cancer, Angew. Chem., Int. Ed. Engl. 60 (2021) 4657–4665.
[15] Y. Wang, Y.Z. Li, J. Chen, H.M. Liu, Y. Zhou, C.X. Huang, L.J. Liang, Y.J. Liu, X. Z. Wang, Anticancer effect evaluation of iridium(III) complexes targeting mitochondria and endoplasmic reticulum, J. Inorg. Biochem. 239 (2023) 112054.
[16] G. Gupta, S. Cherukommu, G. Srinivas, S.W. Lee, S.H. Mun, BODIPY-based Ru(II) and Ir(III) organometallic complexes of avobenzone, a sunscreen material: potent anticancer agents, J. Inorg. Biochem. 189 (2018) 17–29.
[17] J. Chen, H.M. Liu, Y.C. Chen, H.Y. Hu, C.X. Huang, Y. Wang, L.J. Liang, Y.J. Liu, Iridium(III) complexes inhibit the proliferation and migration of BEL-7402 cells through the PI3K/AKT/mTOR signaling pathway, J. Inorg. Biochem. 241 (2023) 112145.
[18] Y.Y. Gu, H.Y. Wen, Y.Y. Zhang, L. Bai, Y. Zhou, H.W. Zhang, L. Tian, J. Hao, Y. J. Liu, Studies of anticancer activity in vivo and in vitro behaviors of liposomes encapsulated iridium(III) complex, J. Biol. Inorg. Chem. 26 (2021) 109–122.
[19] W.J. Wang, Y.Y. Ling, Y.M. Zhong, Z.Y. Li, C.P. Tan, Z.W. Mao, Ferroptosis-enhanced cancer immunity by a ferrocene-appended iridium(III) diphosphine complex, Angew Chem. Int. Ed. Engl. 61 (2022) e202115247.
[20] W.G. Chen, X.H. Cai, Q. Sun, X.H. Guo, C.M. Liang, H. Tang, H.M. Huang, H. Luo, L.M. Chen, J.C. Chen, Design and synthesis of aptamer-cyclometalated iridium(III) complex conjugate targeting cancer cells, Eur. J. Med. Chem. 236 (2022) 114335.
[21] G. Gupta, P. Kumair, J.Y. Ryu, J. Lee, S.M. Mobin, C.Y. Lee, Mitochondrial localization of highly fluorescent and photostable BODIPY-based ruthenium(II), rhodium(III), and iridium(III) metal complexes, Inorg. Chem. 58 (2018) 8587–8595.
[22] Z. Liu, P.J. Sadler, Organoiridium complexes: anticancer agents and catalysts, Acc. Chem. Res. 47 (2014) 1174–1185.
[23] L.H. Guo, X.Y. Hu, Y.J. Yang, W.Y. An, J. Gao, Q. Liu, Z. Liu, Synthesis and biological evaluation of zwitterionic half-sandwich Rhodium(III) and Ruthenium (II) organometallic complexes, Bioorg. Chem. 116 (2021) 105311.
[24] H.W. Zhang, X.F. Liao, X.Y. Wu, C.L. Shi, Y.Y. Zhang, Y.H. Yuan, W.L. Li, Y.J. Liu, Iridium(III) complexes entrapped in liposomes trigger mitochondria-mediated apoptosis and GSDME-mediated pyroptosis, J. Inorg. Biochem. 228 (2022) 111706.
[25] R. Ramos, J.F. Gilles, R. Morichon, C. Przybylski, B. Caron, C. Botuha, A. Karaiskou, M. Salmain, J. Sobczok-Thépot, Cytotoxic BODIPY-Appended Half-Sandwich iridium(III) complexes forms protein adducts and induces ER stress, J. Med. Chem. 64 (2021) 16675–16686.
[26] L. Bai, W.D. Fei, Y.Y. Gu, M. He, F. Du, W.Y. Zhang, L.L. Yang, Y.J. Liu, Liposomes encapsulated iridium(III) polypyridyl complexes enhance anticancer activity in vitro and in vivo, J. Inorg. Biochem. 205 (2020) 111014.
[27] F. Du, L. Bai, M. He, W.Y. Zhang, Y.Y. Gu, H. Yin, Y.J. Liu, Design, synthesis and biological evaluation of iridium(III) complexes as potential antitumor agents, J. Inorg. Biochem. 201 (2019) 110822.
[28] Y.H. Yuan, C.L. Shi, X.Y. Wu, W.L. Li, C.X. Huang, L.J. Liang, J. Chen, Y. Wang, Y. J. Liu, Synthesis and anticancer activity in vitro and in vivo evaluation of iridium (III) complexes on mouse melanoma B16 cells, J. Inorg. Biochem. 232 (2022) 111820.
[29] T. Mosmann, Rapid colorimetric assay for cellular growth and survival: application to proliferation and cytotoxicity assays, J. Immunol. Methods 65 (1983) 55–63.
[30] C.X. Huang, Y.H. Yuan, G.C. Li, S. Tian, H.Y. Hu, J. Chen, L.J. Liang, Y. Wang, Y. J. Liu, Mitochondria-targeted iridium(III) complexes encapsulated in liposome induce cell death through ferroptosis and gasdermin-mediated pyroptosis, Eur. J. Med. Chem. 266 (2024) 116112.
[31] H.L. Roderick, S.J. Cook, Ca^{2+} signaling checkpoints in cancer: remodelling Ca^{2+} for cancer cell proliferation and survival, Nat. Rev. Cancer 8 (2008) 361–375.
[32] Y.P. Ow, D.R. Green, Z. Hao, T.W. Mak, Cytochrome c: functions beyond respiration, Nat. Rev. Mol. Cell Biol. 9 (7) (2008) 532–542.
[33] J. Pessoa, Cytochrome c in cancer therapy and prognosis, Biosci. Rep. 42 (2022) BSR20222171.
[34] R.S. Hotchkiss, A. Strasser, J.E. McDunn, P.E. Swanson, Cell death. N. Engl, J. Med. Chem. 361 (2009) 1570–1583.
[35] A. Hunt, G. Evan, Till death us do part, Science 293 (2001) 1784–1785.
[36] D.H. Manz, N.L. Blanchette, B.T. Paul, F.M. Torti, S.V. Torti, Ann. N. Y. Acad. Sci. Iron and Cancers: Recent Insights 1368 (2016) 149–161.
[37] Y. Xie, W. Hou, X. Song, Y. Yu, J. Huang, X. Sun, R. Kang, D. Tang, Cell Death Differ. Ferroptosis: Process Funct. 23 (2016) 369–379.
[38] X.C. Li, J.Y. Zeng, Y.P. Liu, M.S. Liang, Q.R. Liu, Z. Li, X.J. Zhao, D.F. Chen, Inhibitory effect and mechanism of action of quercetin and quercetin Diels-Alder anti-dimer on erastin-induced ferroptosis in bone marrow-derived mesenchymal stem cells, Antioxidants 9 (2020) 205.
[39] H. Yuk, M. Abdullah, D. Kim, H. Lee, S. Lee, Necrostatin-1 prevents ferroptosis in a RIPK1- and Ido-independent manner in hepatocellular carcinoma, Antioxidants 10 (2021) 1347.
[40] S. Sprouse, K.A. King, P.J. Spellane, R.J. Watts, Photophysical effects of metal-carbon σ bonds in ortho-metalated complexes of iridium(III) and rhodium(III), J. Am. Chem. Soc. 106 (1985) 6647–6653.
[41] G.M. Sheldrick, SHELXL-97, Program for Crystal Structure Refinement, University of Gttingen, Germany, 1997.